Bioactive Materials 41 (2024) 257–270

Contents lists available at ScienceDirect

Bioactive Materials

journal homepage: www.keaipublishing.com/en/journals/bioactive-materials

A multifunctional scaffold that promotes the scaffold-tissue interface integration and rescues the ROS microenvironment for repair of annulus fibrosus defects

Runze Zhao [a,b,1], Feng Han [a,c,1], Qifan Yu [a], Zhuang Zhu [a], Zhengdong Tu [a,d], Tingting Xia [e,**], Bin Li [a,f,*]

[a] Medical 3D Printing Center, Orthopedic Institute, Department of Orthopedic Surgery, The First Affiliated Hospital, MOE Key Laboratory of Geriatric Diseases and Immunology, School of Biology and Basic Medical Sciences, Suzhou Medical College, Soochow University, Suzhou, Jiangsu, 215000, China
[b] Center of Translational Medicine and Clinical Laboratory, The Fourth Affiliated Hospital to Soochow University, Suzhou, 215028, China
[c] Division of Spine Surgery, Department of Orthopedic Surgery, Nanjing Drum Tower Hospital, Affiliated Hospital of Medical School, Nanjing University, Nanjing, 210000, China
[d] Second Department of Orthopaedics, Suzhou Kowloon Hospital, Shanghai Jiaotong University Medical School, Suzhou, 215127, China
[e] Institute of Clinical Medicine Research, Suzhou Hospital, Affiliated Hospital of Medical School, Nanjing University, Suzhou, 215153, China
[f] Collaborative Innovation Center of Hematology, Soochow University, Suzhou, Jiangsu, 215000, China

ARTICLE INFO

Keywords:
Annulus fibrosus
Scaffold-tissue integration
Lysyl oxidase
Reactive oxygen species regulation
Manganese dioxide nanoparticles

ABSTRACT

Due to the limited self-repair ability of the annulus fibrosus (AF), current tissue engineering strategies tend to use structurally biomimetic scaffolds for AF defect repair. However, the poor integration between implanted scaffolds and tissue severely affects their therapeutic effects. To solve this issue, we prepared a multifunctional scaffold containing loaded lysyl oxidase (LOX) plasmid DNA exosomes and manganese dioxide nanoparticles (MnO_2 NPs). LOX facilitates extracellular matrix (ECM) cross-linking, while MnO_2 NPs inhibit excessive reactive oxygen species (ROS)-induced ECM degradation at the injury site, enhancing the crosslinking effect of LOX. Our results revealed that this multifunctional scaffold significantly facilitated the integration between the scaffold and AF tissue. Cells were able to migrate into the scaffold, indicating that the scaffold was not encapsulated as a foreign body by fibrous tissue. The functional scaffold was closely integrated with the tissue, effectively enhancing the mechanical properties, and preventing vascular invasion, which emphasized the importance of scaffold-tissue integration in AF repair.

1. Introduction

The intervertebral disc (IVD) is a cushion located between the vertebrae in the spinal column. The IVD provides shock absorption and allows for flexibility and spinal movement [1–3]. Normal IVDs are composed of a gel-like central nucleus pulposus (NP), surrounded by a tough outer annulus fibrosus (AF) [4,5]. The AF provides support and stability to the disc, helping to distribute stress and load across the disc to maintain the IVD shape and prevent the NP from leaking [2,6,7]. Defects in AF can induce IVD herniation, and finally lead to low back pain (LBP). Epidemiological studies indicates that LBP is the leading cause of the loss of worldwide productivity in 195 countries [8,9]. The socioeconomic burden of LBP is estimated to be exceed $100 billion in the United States [10]. Therefore, repairing a damaged AF is critical for alleviating IVD degeneration [11,12].

Discectomy is the most common strategy for IVD herniation. However, the postoperative results of discectomy are not satisfactory, and 25% of patients require reoperation, which seriously affects the patient's quality of life [13,14]. In this context, tissue engineering technologies using biomimetic scaffolds to recapture AF structure and function are a promising alternative strategies for AF repair. Gluais et al. prepared an aligned polycaprolactone (PCL) microfiber scaffold using

Peer review under responsibility of KeAi Communications Co., Ltd.
* Corresponding author. Rm 201 Bldg Jiwu, Soochow University (North Campus), 178 Ganjiang Rd, Suzhou, Jiangsu, 215007, China.
** Corresponding author.
E-mail addresses: xtt_92@126.com (T. Xia), binli@suda.edu.cn (B. Li).
[1] These authors equally contributed to this study.

https://doi.org/10.1016/j.bioactmat.2024.03.007
Received 17 October 2023; Received in revised form 4 March 2024; Accepted 7 March 2024

electrospinning, and evaluated its effect in sheep lumbar discs. The results showed the scaffold aligned with the collagen fiber organization within each lamella [15]. Shamsah et al. mixed PCL and poly(L-lactic) acid (PLLA) in different ratios to prepare a structured biomimetic AF scaffold. The results showed that the 50:50 ratio of PCL and PLLA had characteristics similar to those of human AF and maintained AF cells adhesion and proliferation [16]. Despite their promising results in repairing AF, biomimetic scaffolds still face challenges in clinical application partly because of the poor integration with native AF. If the implanted scaffolds cannot achieve stable integration with the surrounding tissue, they may fail to repair the defective tissues. Cracks between the scaffold and tissue may also promote blood vessel and nerve infiltration, which cause chronic discogenic pain and secrete pro-inflammatory cytokines such as interleukins and tumor necrosis factor alpha (TNF-α) [17,18]. Collagen cross-linking at the scaffold-tissue interface can facilitate a tight connection between the implanted scaffold and the AF, enhancing the interface's mechanical properties [19]. Hence, promoting the cross-linking of collagen is a possible solution to enhance scaffold-tissue integration.

Lysyl Oxidase (LOX) is a copper-dependent amine oxidase that catalyzes the cross-linking of collagen and elastin in the ECM that is secreted by various cell types. LOX plays a crucial role in maintaining the stability and strength of the ECM [20–23]. Our previous study indicated that LOX relieved the process of intervertebral disc degeneration (IDD) [24]. However, exogenous proteins may be inactive in vivo because of the complex microenvironment, making LOX gene transfection into AF cells (AFCs) a more favorable alternative. Increasing evidence indicates that exosomes produced by mesenchymal stem cells (MSCs)have shown significant potential for gene delivery applications [25,26]. Exosomes are tiny lipid-bilayer enclosed vesicles, ranging in diameter from 30 to 150 nm, that are internalized and secreted by cells. They transport various active substances and serve as natural intercellular communication mediators. Zha et al. developed an engineered exosome loaded with VEGF pDNA for inducing vascularized osteogenesis [27]. Therefore, using MSC-derived exosomes loaded with LOX pDNA can enhance the exploitation of LOX in promoting ECM cross-linking.

Moreover, tissue damage is frequently accompanied by excessive reactive oxidative stress (ROS) [28,29]. ROS can lead to inflammation, further upregulating matrix metalloproteinases expression. This, in turn, triggers the ECM degradation, ultimately reducing the cross-linking effectiveness of LOX on the ECM [29]. Additionally, ROS has been shown to induce IVD degeneration variously, including angiogenesis, inflammation, apoptosis, aging etc. [29–31]. Therefore, increasing number of researchers are combining antioxidants and scaffolds for tissue repair. The main types of ROS are hydrogen peroxide (H_2O_2), superoxide anions (O_2-), and hydroxyl radicals (HO•) [32,33]. Antioxidant compounds, such as manganese dioxide (MnO_2), are commonly used to remove excess ROS [34,35]. Kumar et al. fabricated MnO_2 nanoparticles (MnO_2 NPs) with a diameter of less than 20 nm and injected them into an osteoarthritis (OA) knee joint. The results demonstrated that the MnO_2 NPs significantly scavenge ROS in OA, inhibited the inflammatory response, and protected the articular cartilage [36]. Therefore, using MnO_2 NPs to scavenge excess ROS in defected areas can significantly enhance LOX effectiveness in promoting scaffold-tissue integration.

This study aimed to improve scaffold-tissue integration by promoting collagen cross-linking and ROS scavenging for effective AF repair. To promote collagen cross-linking, we first fabricated aligned PCL nanofiber scaffolds that mimic the AF structure through electrostatic spinning. To increase PCL biocompatibility and provide modification sites, we utilized layer-by-layer assembly to deposit silk fibroin (SF) onPCL nnofiber surface (SF/PCL) [37]. After that, these scaffolds were decorated with dibenzocyclooctyne (DBCO). Second, MSC-derived exosomes were decorated with azide and loaded with LOX pDNA. The LOX pDNA-loaded exosomes were grafted to the SF/PCL scaffold surface via a click chemistry reaction. To scavenge ROS, we fabricated MnO_2 NPs, and the MnO_2 NPs were absorbed onto the SF/PCL scaffold surface via physical adsorption (Scheme 1). Our in vitro study showed that this multifunctional scaffold had excellent biocompatibility, efficiently delivered LOX pDNA to AFCs, and elicited high LOX expressio. The scaffold was also highly effective in removing ROS from AFCs. The repair effect of multifunctional scaffolds on AF was evaluated using a rat tail box model. This multifunctional scaffold also prevented blood vessels ingrowth. The results indicated that this multifunctional scaffold could efficiently remove ROS and inhibit inflammation. LOX played a key role in enhancing scaffold-AF tissue integration and maintaining the mechanical properties of the scaffold-AF tissue boundar.

2. Materials and methods

2.1. Extraction and culture of AF cells

Eight-week-old male rats underwent pentobarbital execution. The dorsal hairs of the rats were sterilized with 75% ethanol. The lumbar and caudal vertebrae were then surgically removed under aseptic conditions, and the attached soft tissues were removed. The intact AF tissue was extracted and placed in a medium containing 5% penicillin/streptomycin. After enzyme digestion and filtering, the tissue was centrifuged, resuspended in a complete medium (DMEM/F12 medium with 10% FBS, 1% penicillin-streptomycin), and incubated at 37 °C with 5% CO_2 in an incubator. The culture medium was changed every two days, and cells were passaged when they reached approximately 80% growth on the culture dish.

2.2. Preparation of PCL nanofiber scaffolds

To prepare a 10% (W/V) PCL solution, 0.5 g of PCL was dissolved in 5 mL of hexafluoroisopropanol. The solution was drawn into a 10 mL syringe and electrospun using a micro syringe pump at a rate of 1 mL/h and a voltage of 15 kV. The syringe needle was positioned 15 cm from the collector and the drum collector speed was set to 2500 r/min.

2.3. Silk extraction

To prepare the SF extract, 6–8 g of cocoons were cut, boiled with 0.02 M sodium carbonate solution at 98 °C for 1 h, and then soaked and cleaned with deionized water five times. The dried SF was weighed (2 g) and dissolved in 10 mL of a 9.3 M lithium bromide solution for 4 h at 60 °C. The dissolved SF solution was dialyzed with deionized water for three days and filtered to obtain the final SF solution.

2.4. Preparation of fluorescein isothiocyanate (FITC)-labeled SF

The concentration of the SF solution was adjusted to 2% and dialyzed in MES buffer (0.1 M with 0.9% NaCl) at pH 5.6 for 24 h. 1-(3-Dimethylaminopropyl)-3-ethylcarbodiimide hydrochloride (EDC) (80 mg) and N-Hydroxysuccinimide (NHS) (220 mg) were added to the SF solution and stirred for 15 min. The reaction was then stopped by adding 20 μL of β-mercaptoethanol. Ethylenediamine (2 μL) was added for 2 h at room temperature, and the reaction system was dialyzed in 4-Morpholineethanesulfonic acid (MES) buffer for 24 h to remove unreacted reagents. The solution was then treated with 8.23 mg of FITC under light-proof conditions and stirred slowly for 2 h. After dialysis in deionized water for 24 h under light-proof conditions, the resulting solution was stored at 4 °C.

2.5. Preparation of SF/PCL

The concentration of the SF solution was adjusted to 1 mg/mL, the PCL scaffold was cut into 2 cm × 2 cm pieces, and washed twice with deionized water for 5 min each time. A volume of 2 mL of 0.5 mg/mL

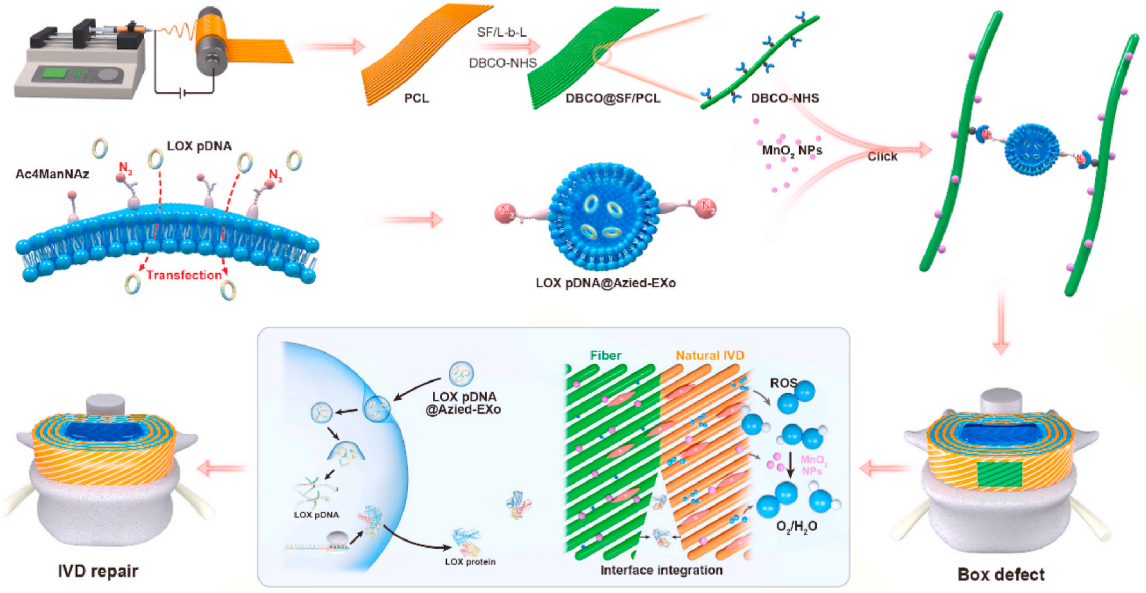

Scheme 1. We designed and prepared a multifunctional scaffold, including an engineered exosome loaded with LOX pDNA and $_2MnO_2$ NPs. The exosomes serve as efficient carriers for delivering LOX pDNA into AFCs, facilitating ECM cross-linking and promoting seamless integration between the scaffold and the surrounding tissue. Additionally, MnO_2 NPs efficiently eliminate ROS and inhibit inflammation. This multifunctional scaffold thus holds significant promise for AF repair.

branched polyetherimide (bPEI) (25 kDa) solution was added and shaken for 15 min, washed with 3 mL of deionized water twice for 5 min each time; 2 mL of 1 mg/mL SF solution was added and shaken for 10 min at 4 °C, then washed three times with deionized water. After that, 2 mL of 90% methanol was added for 15 min to increase β sheets foldin, and the scaffold was dried under 5–15 kPa nitrogen for 5 min to increase the hydrophobicity between the layers. The SF assembly steps were repeated to attain the desired number of layers.

2.6. Characterizations of the scaffolds

Fourier transform infrared spectroscopy (FTIR) (PerkinElmer Frontier, PerkinElmer, Waltham, MA, USA) was employed to determine the absorption spectra of PCL, SF, SF/PCL-2L, SF/PCL-4L, and SF/PCL-8L.

The prepared scaffolds underwent several analyses. The morphology was examined using SEM (FEI, USA). The hydrophilicities of the scaffolds were evaluated by measuring the dynamic water contact angle using a contact angle analyzer (JGW360B, China). Elemental analysis was evaluated using EDS.

To assess the mechanical properties of the scaffolds, scaffolds of a 15.0 × 3.0 × 0.1 mm size were prepared prior to a tensile test. The mechanical properties were analyzed uising load-deformation tests with a speed of 2.5 mm/min using an Instron (Shanghai Hengyi Precision Instruments Co., China).

2.7. Preparation of LOX pDNA-loaded exosomes (LOX-Exo)

The transfection of rat mesenchymal stem cells (rBMSCs) with GFP-labeled LOX pDNA was performed using a transfection kit. The cells were washed with PBS after 12 h of transfection and kept in a serum-free medium for another 24 h. The supernatant was then collected and centrifuged in three steps at 2000 g, 10000 g, and 100000 g to separate the LOX pDNA-loaded exosomes. The supernatant was discarded, and the residual precipitate was resuspended in 1 mL of PBS. Nanoparticle tracking analysis (NTA, Malvern Panalytical, UK) was used to measure the size distribution of LOX-Exo. Agarose gel electrophoresis was used to verify that LOX pDNA was successfully loaded into the exosomes.

2.8. Preparation and characterization of MnO2 NPs

MnO_2 NPs were prepared using a 30-min redox reaction involving potassium permanganate (Acros Organics in Geel, Belgium) and poly (allylamine hydrochloride) (Alfa Aesar in Ward Hill, MA, USA), both of which were used at a 1:1 concentration ratio and mixed with water [34,38,39].

The UV–visible absorption spectrum of 100 μg/mL potassium permanganate ($KMnO_4$) and MnO_2 NPs in water was measured using a spectrophotometer (Biotek Synergy HT, Winooski, Vermont, USA) within a range of 300–900 nm. The zeta potential of MnO_2 NPs was assessed using dynamic light scattering (DLS; Malvern Panalytical, UK). The particles were suspended in water at room temperature. Transmission electron microscopy (TEM) (Tecnai™ FEI Spirit TEM 120 kV, ThermoFisher Scientific, Waltham, MA, USA) was utilized to image the MnO_2 NP, and ImageJ was employed to analyze the images. Additionally, the scavenging capacity of MnO_2 NPs in concentrations ranging from 0 to 10 μg/mL was evaluated for 100 μM H_2O_2 after 1h in PBS using H_2O_2 colorimetric detection kits (TMB ELISA substrate, Nanjing Jiancheng).

Initially, AFCs were seeded onto plates for 12 h. Following this, these cells were treated with 100 μm H_2O_2 and 10 μg/mL MnO_2 NPs and allowed to incubate for a further 12h. Subsequently, DCFH-DA was used to evaluate the intracellular ROS level of AFCs. To evaluate the anti-ROS effect of F-Exo@SF/PCL, AFCs were also seeded onto different scaffolds, after which they were treated with 100 μm H_2O_2 following a 12h incubation period. The fluorescence images were captured using an inverted fluorescence microscope (EVOS, USA).

2.9. Preparation of multifunctional LOX-Exo@SF/PCL scaffold (F-Exo@SF/PCL)

The LOX-Exos were successfully attached to the oriented SF/PCL nanofiber scaffolds using a SPAAC click chemistry reaction system. To achieve this, the NHS Ester-labeled dibenzocyclooctyne (DBCO) was initially reacted with the SF amino terminus via an acylation reaction. The DBCO was dissolved in dimethyl sulfoxide (DMSO) at a concentration of 10 μM, and the SF/PCL scaffold was then soaked in the DBCO solution overnight at 4 °C. Afterward, the LOX pDNA was transfected

into rBMSCs using a transfection kit, and with varying concentrations (0 μM, 5 μM, 10 μM, and 20 μM) of Ac4ManNAz added to the culture medium. The cells were washed three times with PBS after 24 h and then incubated in a serum-free culture medium for another 24 h. The azide-modified LOX-Exos were harvested using ultracentrifugation and co-incubated with a DBCO-pretreated SF/PCL scaffold, undergoing a click reaction at 37 °C for 1 h. After PBS washing, the scaffold was incubated with 10 μg/mL of MnO_2 NPs solution for 1 h to create a multifunctional LOX-Exo@SF/PCL scaffold (F-Exo@SF/PCL).

2.10. Cell viability analysis

AFCs were grown on nanofibrous scaffolds for 1, 2, and 3 days. Then, a 10% CCK-8 solution was added and incubated for 3 h (Dojin Laboratories, Kumamoto, Japan). The cellular viability was evaluated by measuring the absorbance at 490 nm using a microplate reader (BioTek Instruments, USA).

2.11. Gene expression analysis

Total RNA from AFCs was extracted using TRIzol reagent (Invitrogen, Carlsbad, CA, USA) and analyzed through real-time quantitative polymerase chain reaction (RT-qPCR). The extracted RNA concentration was assessed using a NanoDrop 2000 spectrophotometer (Thermo Fisher Scientific, Waltham, MA, USA). Afterward the RNA was converted into first-strand cDNA for use in the quantitative polymerase chain reaction. The primer sequences for the relevant genes were acquired from Sangon Biotech (Shanghai, China) and are listed in Table S1. Normalization of the relative mRNA expression for each gene was conducted using Gapdh, and computed using the $2^{-\Delta\Delta Ct}$ method.

2.12. Western blot analysis

Proteins were extracted from AFCs on the scaffolds and analyzed using a BCA kit (Beyotime, Beijing, China) to determine their concentrations. Diluted primary antibodies were incubated with the proteins overnight at 4 °C, and then treated with the corresponding secondary antibodies at room temperature for 1 h. Protein detection was carried out through autoradiography (Bio-Rad, Hercules, CA, USA), and the grayscale value was quantified using Image J. The information on primary antibodies used in this study is listed in Table S2.

2.13. Immunofluorescence

The AFCs were fixed using 4% paraformaldehyde, followed by permeabilization with 0.3% Triton X-100 in PBS for 15 min. To prevent nonspecific binding, the cells were then immersed in 2% BSA for 2 h at room temperature. The primary antibodies were incubated with the cells at 4 °C overnight, and labeled with Alexa Fluor 488 secondary antibodies (1:1000, Abcam Cambridge, UK). TRITC-phalloidin diluent (1:300, Yeasen, Shanghai, China) was employed for cytoskeleton staining for 30 min, while 4′, 6-diamidino-2-phenylindole (DAPI) (Beyotime, Beijing, China) was used to stain the nuclei. Images were captured using a fluorescence microscope (Carl Zeiss Microscopy, Thornwood, NY). The information on primary antibodies used for immunofluorescence is listed in Table S3.

2.14. Animal study

All procedures were conducted according to the NIH Guide for the Care and Use of Laboratory Animals and were approved by the Institutional Animal Care and Use Committee of Soochow University (SUDA20220913A01). A total of 48 Sprague Dawley (SD) rats aged 10–12 weeks with a weight of approximately 350 g were used for this experiment. The rats were anesthetized through intraperitoneal injection of pentobarbital and, upon becoming anesthetized, were positioned in a prone posture. Standard disinfection and towel placement were carried out at the surgical site. A 3 cm longitudinal incision was made along the midline of the posterior portion of the tail. The skin, subcutaneous tissue, and fascia were sequentially cut, and the ligaments in the tail were isolated, allowing for lateral pulling to expose the disc completely.

Four groups were formed for this study: (1) a sham group, (2) a box annulotomy without the implantation of materials (defect group), (3) a box annulotomy with the implantation of the Exo@SF/PCL scaffold (Exo@SF/PCL), (4) a box annulotomy with the implantation of the functional Exo@SF/PCL scaffold (F-Exo@SF/PCL). The Co7-8 and Co8-9 IVD segments were chosen to construct the AF box defect model [40]. Briefly, a 2.0 mm × 1.0 mm and 1.0 mm deep box defect was carefully cut in the AF. Then, the custom scaffolds were covered on the defected sites. After 8 weeks, the rats were sacrificed under general anesthesia via intraperitoneal injection of pentobarbital. Caudal spines were collected and instantly fixed with 10% paraformaldehyde for 1 day at room temperature.

2.15. Imaging of H_2O_2 at AF defect sites

Lipo@HRP&ABTS nanoprobes were used to detect the H_2O_2 level in vivo. The nanoprobes were locally injected into the AF defect in 50 μL volumes, and the H_2O_2 level was observed and measured using a Vevo LAZR Imaging System (FUJIFILM VisualSonics Inc.) after 15 min.

2.16. Imaging analysis

The sagittal position of the caudal spines of the rats were imaged using X-rays while they were in a supine position. The disc height index (DHI) was calculated for comparison between groups using the following formula: DHI = (2 x sum of anterior, middle, and posterior edge height of intervertebral space)/(sum of anterior, middle, and posterior height of adjacent vertebral bodies). The magnetic resonance imaging (MRI) was performed after the surgery to evaluate T2 signal changes in the NP using a 1.5T MRI scanner (Magnetom Essenza, Siemens Medical Solutions, Erlangen, Germany).

2.17. Histological analysis

The collected samples were fixed in a 10% formaldehyde solution and then decalcified in a 14% ethylenediaminetetraacetic acid (EDTA) solution. After that, the discs were embedded in an optimal cutting temperature compound, then flash-frozen in liquid nitrogen, and sectioned into 9 μm sections. Tissue histology was examined using hematoxylin and eosin (H&E) staining. Additionally, the expression and distribution of proteoglycan and collagen were determined through safranin O/fast green (SO/FG) and Sirius red staining.

To detect immunofluorescence, all slices were blocked with a solution containing 10% donkey serum, 0.3% Triton X-100, and 1% BSA for 2 h. These specimens were then incubated with primary antibodies against collagen I or CD31 overnight at 4 °C. After washing with PBS, appropriate secondary antibodies and DAPI were added to visualize the cell nuclei and immunoreactivity products. The slices were then examined using a fluorescence microscope (Carl Zeiss Microscopy, Thornwood, NY).

2.18. Mechanical analysis

The fresh harvest IVD was sectioned horizontally with 30 μm thickness using a frozen tissue section (CM3050 S, Leica, Nussloch, Germany). The elastic modulus of the scaffold-tissue integration interface was conducted with an atomic force microscope (AFM) scanner ((JPK Instruments, Nano Wizard II, Germany). The elastic modulus was measured in the force-volume mode. The probe of spring constant was 0.06 N/m (Olympus Corporation, Olympus, Tokyo, Japan) [41].

2.19. Statistical analysis

Quantitative data are reported as mean ± standard deviation (SD) based on at least three independent repetitions within each group. Statistical analysis was conducted using one-way ANOVA methods, followed by Tukey's HSD post hoc test using GraphPad Prism 8 software. A statistically significant difference is defined as $p < 0.05$.

3. Results

3.1. Preparation and characterization of azide-modified LOX pDNA-loaded exosomes

The schematic diagram of azide-modified exosomes is shown in Fig. 1A. BMSCs were co-cultured with Ac4ManNAz. The azide group can be transported to the cell membrane surface via glycoengineering. Meanwhile, LOX pDNA was transferred into BMSCs using a commercial transfection kit to obtain azide-modified LOX pDNA-laden exosomes. The expression of exosome-specific markers CD63 and TSG101 was detected in the collected substances using Western blotting (Fig. 1B). The result of agarose gel electrophoresis demonstrated that LOX pDNA was successfully transferred into the exosomes after electroporation (Fig. 1C). NTA analysis further confirmed that neither N3 modification nor LOX pDNA loading changed the exosomes' size (Fig. 1D). These results indicate that we successfully obtained azide-modified LOX pDNA-loaded exosomes.

3.2. Preparation and characterization of SF/PCL scaffolds

The aligned PCL scaffold was prepared using electrostatic spinning, and then the SF was deposited on the PCL nanofiber surface using layer-by-layer self-assembly. SEM analysis revealed that the surface of pure PCL nanofiber surface was smooth, and the fiber surface was gradually roughened with an increase in the number of SF deposited layers (Fig. 2A). The SF assembly was mainly accomplished through the β-sheet formation, which was confirmed using FTIR analysis, showing a transferred characteristic peak of the β-sheet structure from 1650 cm^{-1} to 1627 cm^{-1} in SF/PCL compared with pure SF (Fig. 2B). In addition, the fluorescence signal of SF labeled with FITC displayed more strongly as the number of SF-deposited layers increased, confirming the successful preparation of SF/PCL scaffolds (Fig. 2C and D). These results demonstrated that SF/PCL scaffolds were successfully prepared. Moreover, SF deposition did not significantly affect the mechanical properties of these scaffolds (Fig. S1). The contact angle assay results demonstrated a significant increase in scaffold hydrophilicity with an increasing number of SF-deposited layers (Fig. S2).

3.3. Preparation and characterization of multifunctional Exo@SF/PCL scaffold (F- Exo@SF/PCL)

The click chemistry schematic diagram is shown in Fig. 2E. The SPAAC system was used to graft the LOX pDNA-loaded exosomes onto SF/PCL scaffolds. 1) NHS-DBCO was grafted onto SF/PCL scaffolds using the amide reaction. 2) The azide-exosomes were then pre-labeled using DiI and incubated with DBCO-modified SF/PCL scaffolds for 1 h at 37 °C. Different concentrations of Ac4ManNAz were used to determine the reaction's grafting efficiency, and the results showed that 10 μM Ac4ManNAz exhibited the optimal grafting efficiency (Fig. 2F, G and Fig. S3). After exosome grafting, SEM analysis of the SF/PCL and Exo@SF/PCL nanofibers morphologies showed an irregular substance deposition on the nanofiber surface (Fig. 2H). Meanwhile, MnO_2 NPs were prepared according to the previous study, in which $KMnO_4$ was reduced in the presence of the cationic polyelectrolyte poly-(allylamine hydrochloride) (PAH) (Fig. S4A). The generated MnO_2 NPs showed a positive potential (Fig. S4B), and their average size was around 10 nm (Fig. S4C). Consistent with the previous study, the MnO_2 NPs exhibited good dispersion in deionized aqueous solution, but agglomerated and precipitated in salt ion solution (e.g., PBS) (Fig. S4D) [38]. The MnO_2 NPs were bound to the scaffold surface using physical adsorption, with EDX analysis revealing a uniform MnO_2 NPs distribution on the scaffold

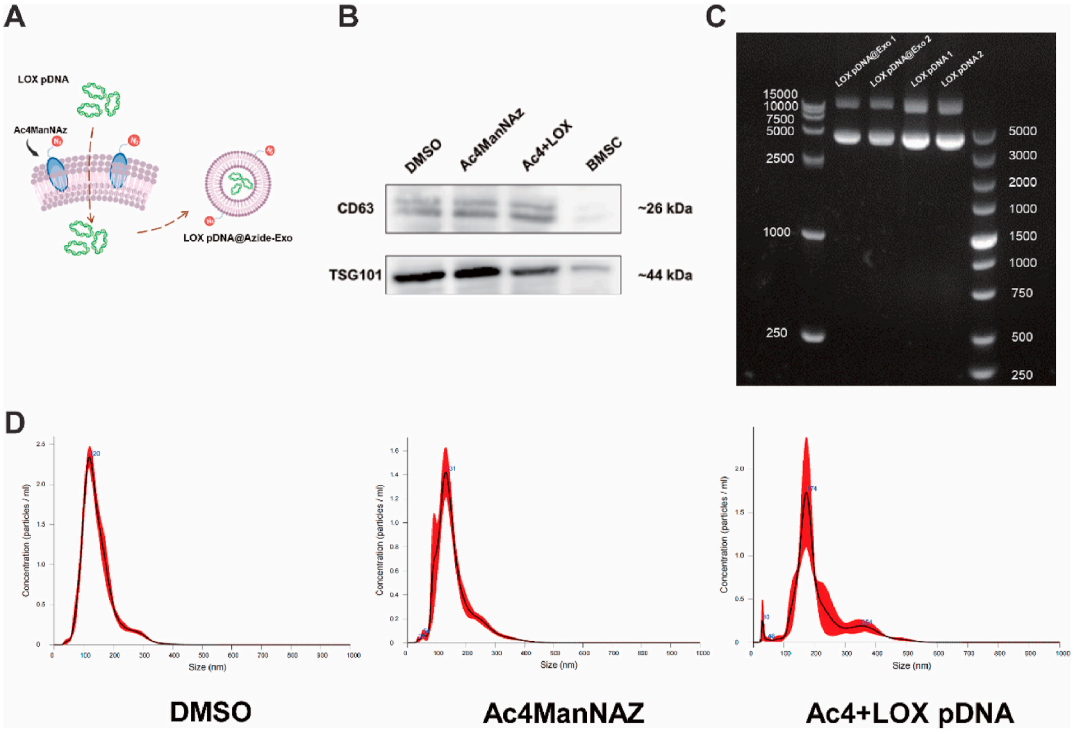

Fig. 1. Preparation and characterization of azide-modified LOX pDNA-loaded exosomes. (A) Schematic illustrations of fabricating azide-modified LOX pDNA-loaded exosomes. (B) Western blot analysis of typical markers of exosome. (C) Agarose gel electrophoresis confirmed the successful loading of LOX pDNA into exosomes. (D) NTA analysis of the size distribution of exosomes from the DMSO group, Ac4ManNAZ treated group, and LOX-pDNA loaded group.

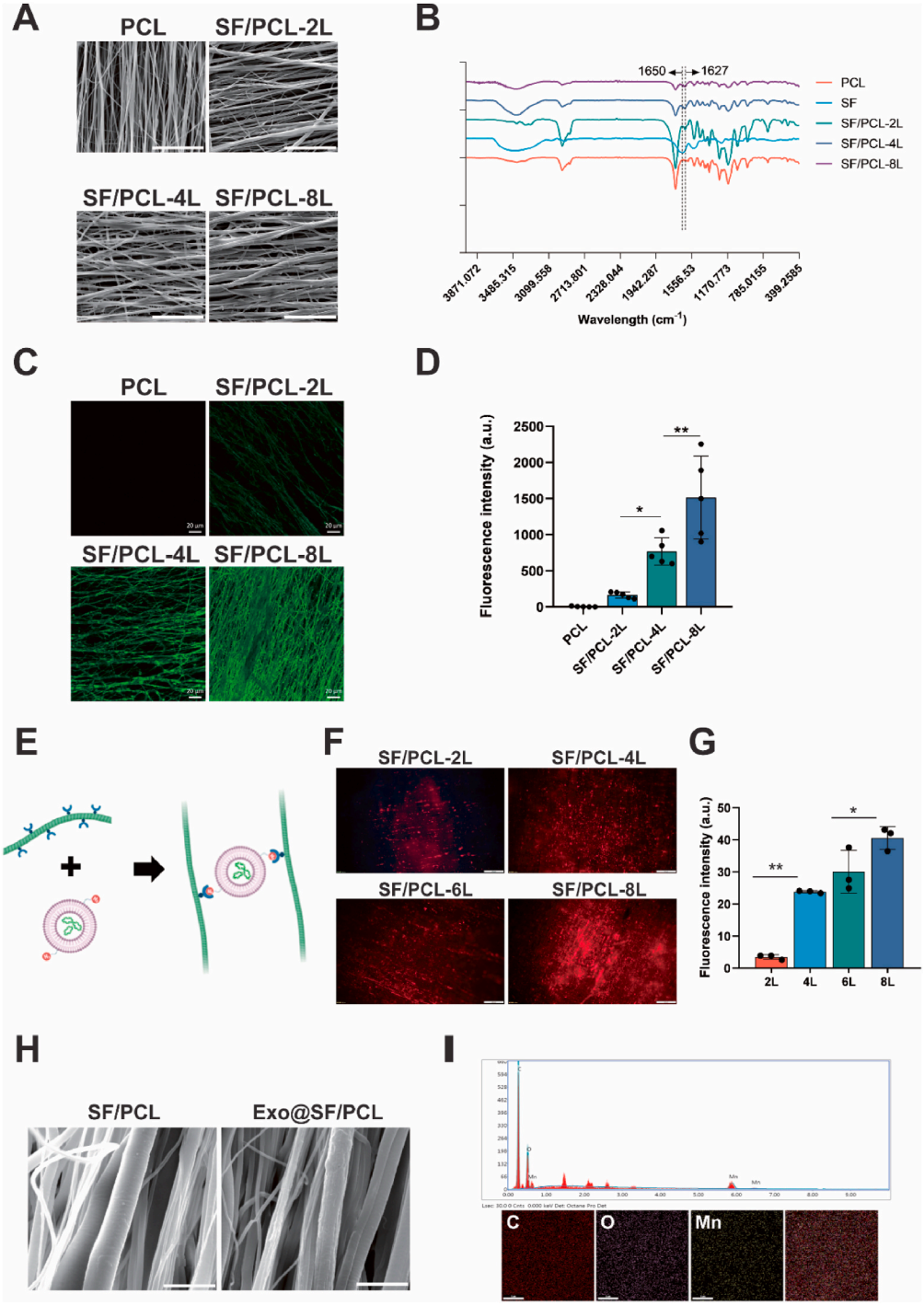

Fig. 2. Preparation and characterization of F-Exo@SF/PCL scaffolds. (A) SEM analysis of the nanofiber morphology of PCL and SF/PCL with different SF layers, scale bar = 20 μm. (B) FTIR analysis of the characteristic absorption peak of β-sheet. (C) FITC labeled SF was confirmed using fluorescence imaging, scale bar = 20 μm. (D) Quantification of fluorescence intensity of PCL and SF/PCL with different SF layers. Data are presented as the mean ± SD, n = 5, $*p < 0.05$, $**p < 0.01$. (E) Schematic illustrations of the azide-modified exosomes clicking SF/PCL nanofibers. (F) The effectiveness of the click reaction was evaluated using DiI-labeled exosomes, scale bar = 200 μm. (G) Quantification of fluorescence intensity analysis of DiI-labeled exosomes clicking onto SF/PCL nanofibers. Data are presented as the mean ± SD, n = 3, $*p < 0.05$, $**p < 0.01$. (H) SEM analysis of the nanofiber morphology of SF/PCL and Exo@SF/PCL, scale bar = 20 μm. (I) EDX elements mapping of C, O, and Mn in the scaffold, scale bar = 1 μm.

(Fig. 2I).

3.4. Biocompatibility and biofunctionality assessment of F-Exo@SF/PCL scaffolds

AFCs were cultured on the scaffold, and cell viability results showed that this multifunctional scaffold had no cytotoxic effect on AFCs (Fig. S5). Moreover, AFCs were demonstrated to grow on this multifunctional scaffold along the direction of fiber alignment via staining the cytoskeleton (Fig. S5). The fluorescence results indicated that the DiI-labeled exosomes were taken up by the AFCs, which was a prerequisite for LOX pDNA transfer into AFCs (Fig. S6). A GFP sequence was

inserted into the LOX pDNA; thereby, the gene transfection efficiency of this multifunctional scaffold was assessed by counting GFP-positive cells. The results indicated that LOX pDNA was successfully transferred into the AFCs through cell endocytosis (Fig. 3A). Different ratios of exosomes were incubated with AFCs, and the result showed that the transfection efficiency was optimal when the ratio of exosomes to the culture medium was 1:1, which resulted in approximately 35% LOX positive AFCs (Fig. S7). In addition, ECM-relative gene and protein expression indicated that LOX had no significant regulatory effect on AFCs ECM production (Fig. 3B and C).

Inflammation-related and antioxidant genes were examined to assess the scavenging effect of the scaffold on ROS. The effect of MnO_2 NPs on H_2O_2 catabolism was evaluated, and the results showed that H_2O_2 was significantly removed with an increasing MnO_2 concentration (Fig. 4A). The detection of intracellular ROS using DCFH-DA further demonstrated the good ROS scavenging effect of MnO_2 NPs (Fig. 4B and C). When AFCs grew on the scaffold, this multifunctional scaffold significantly inhibited LPS-induced inflammation in the cells with the down-regulation of IL-1β and TNF-α (Fig. 4D). Furthermore, this multifunctional scaffold significantly down-regulated the expression of antioxidant gene profiles GPX, MnSOD, ECSOD, and CAT, indicating that the MnO_2 NPs effectively scavenged ROS and reduced the AFCs stress response against ROS (Fig. 4D and E).

3.5. F-Exo@SF/PCL scaffold effectively reduces ROS levels at the injury site of AF

The effect of multifunctional scaffolds on AF repair was evaluated using the rat caudal AF box annulotomy model (Fig. 5A). ROS levels at the injury site were measured using a Lipo@HRP & ABTS probe, which could specifically trace H_2O_2. The result showed that the defect AF exhibited a high ROS level. While the Exo@SF/PCL scaffold did not reduce ROS levels, the F-Exo@SF/PCL scaffold effectively cleared H_2O_2 from the injury site, leading to a decrease in ROS levels (Fig. 5B). Additionally, the TNF-α assay conducted on the AF confirmed that the F-Exo@SF/PCL scaffold effectively reduced inflammation by removing ROS (Fig. 5C).

3.6. F-Exo@SF/PCL scaffold prevents IVD herniation

After 8 weeks of implantation, MRI was used to evaluate the effectiveness of scaffolds in repairing the AF. The results showed that the defect AF could lead to herniation of the NP and cause disc degeneration. However, both the Exo@SF/PCL and F-Exo@SF/PCL scaffolds were effective in preventing NP herniation (Fig. 6A and B). X-ray and statistical analysis of the DHI also confirmed that the scaffolds could prevent IVD herniation (Fig. 6C and D). H&E staining revealed that the border between the AF and the NP was indistinguishable, and the disc

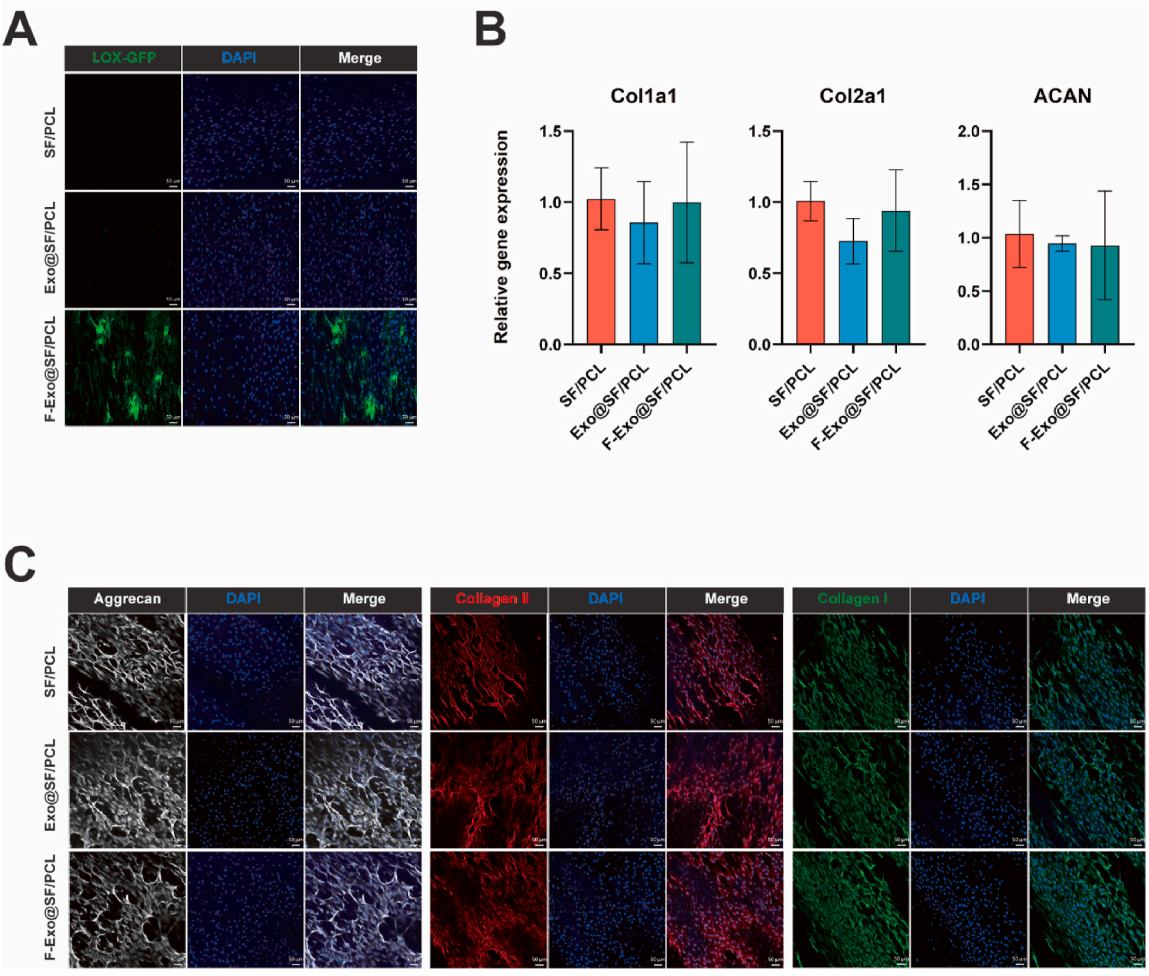

Fig. 3. Biocompatibility and biofunctionality assessment of F-Exo@SF/PCL scaffolds. (A) Detection of LOX pDNA expression in AFCs using GFP fluorescence. Scale bar = 50 μm. (B) Relative gene expression of Col1a1, Col2a1, and ACAN. Data are presented as the mean ± SD, n = 6. (C) Immunofluorescence staining analysis of aggrecan, collagen II, and collagen I expression. Scale bar = 50 μm.

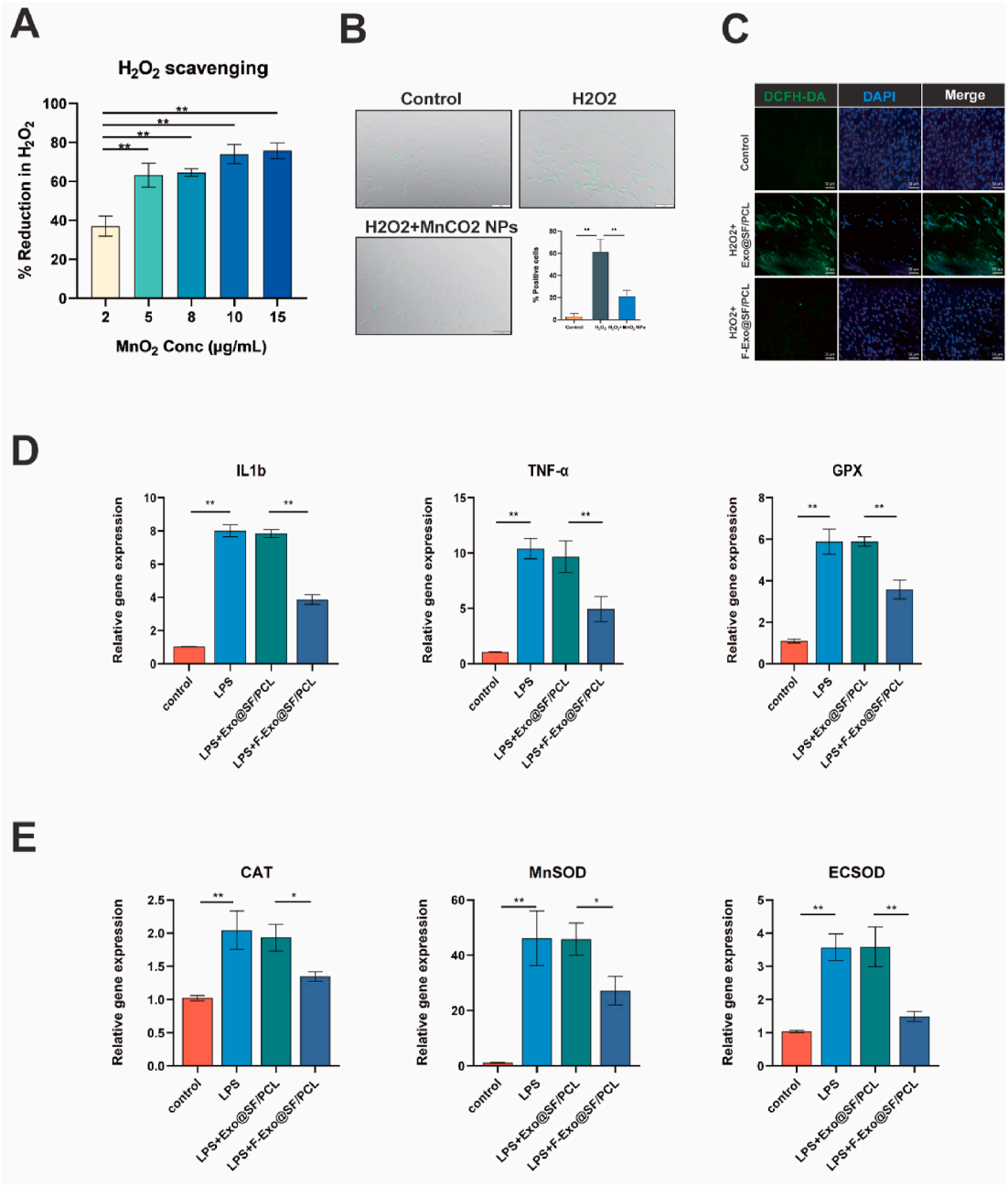

Fig. 4. F-Exo@SF/PCL scaffold effectively reduces ROS levels in vitro. (A, B) Effect of MnO_2 NPs on H_2O_2 scavenging. Scale bar = 200 μm. Data are presented as the mean ± SD, n = 3, $^{**}p < 0.01$. (C) Evaluation of the ROS eliminating effect of F-Exo@SF/PCL scaffold of AFCs using DCFH-DA. Scale bar = 50 μm. (D) Relative gene expression of IL-1β, TNF-α and GPX. Data are presented as the mean ± SD, n = 6, $^{**}p < 0.01$. (E) Relative gene expression of CAT, MnSOD, and ECSOD. Data are presented as the mean ± SD, n = 6, $^{*}p < 0.05$, $^{**}p < 0.01$.

structure was lost in the defect group. While the Exo@SF/PCL scaffold prevented NP leakage, there was poor scaffold-native AF tissue integration, and numerous cracks appeared. In contrast, the F-Exo@SF/PCL scaffold maintained the physiological structure of the AF, and the integration interface between the scaffold and native AF tissue was tightly connected (Fig. 6E). SO/FG staining showed that the AF collagen structure was well arranged in the sham group. In contrast, it was difficult to distinguish the AF structure in the defect group. The implanted Exo@SF/PCL scaffold did not integrate well with the surrounding tissues, and the scaffold was disconnected from the adjacent tissue. However, the F-Exo@SF/PCL scaffold significantly promoted the integration of the scaffold with the surrounding tissue and formed a tight connection due to the effect of LOX (Fig. 6E).

3.7. F-Exo@SF/PCL scaffold promotes scaffold-tissue integration and effectively prevents external vascular invasion

To assess the integration of the scaffold with the AF tissue, various analyses were conducted. Fluorescence results compared the collagen I expression in both Exo@SF/PCL and F-Exo@SF/PCL scaffolds (Fig. 7A). It was worth noting that the presence of cells within the F-Exo@SF/PCL scaffold indicated that cells were capable of migrating from the surrounding tissue into the scaffold. This result demonstrated the integration of the scaffold with the surrounding tissue went well, rather than being recognized as a foreign body and encapsulated in a fibrous capsule. Furthermore, CD31 staining indicated that its expression could only be detected outside the AF in healthy discs, whereas CD31

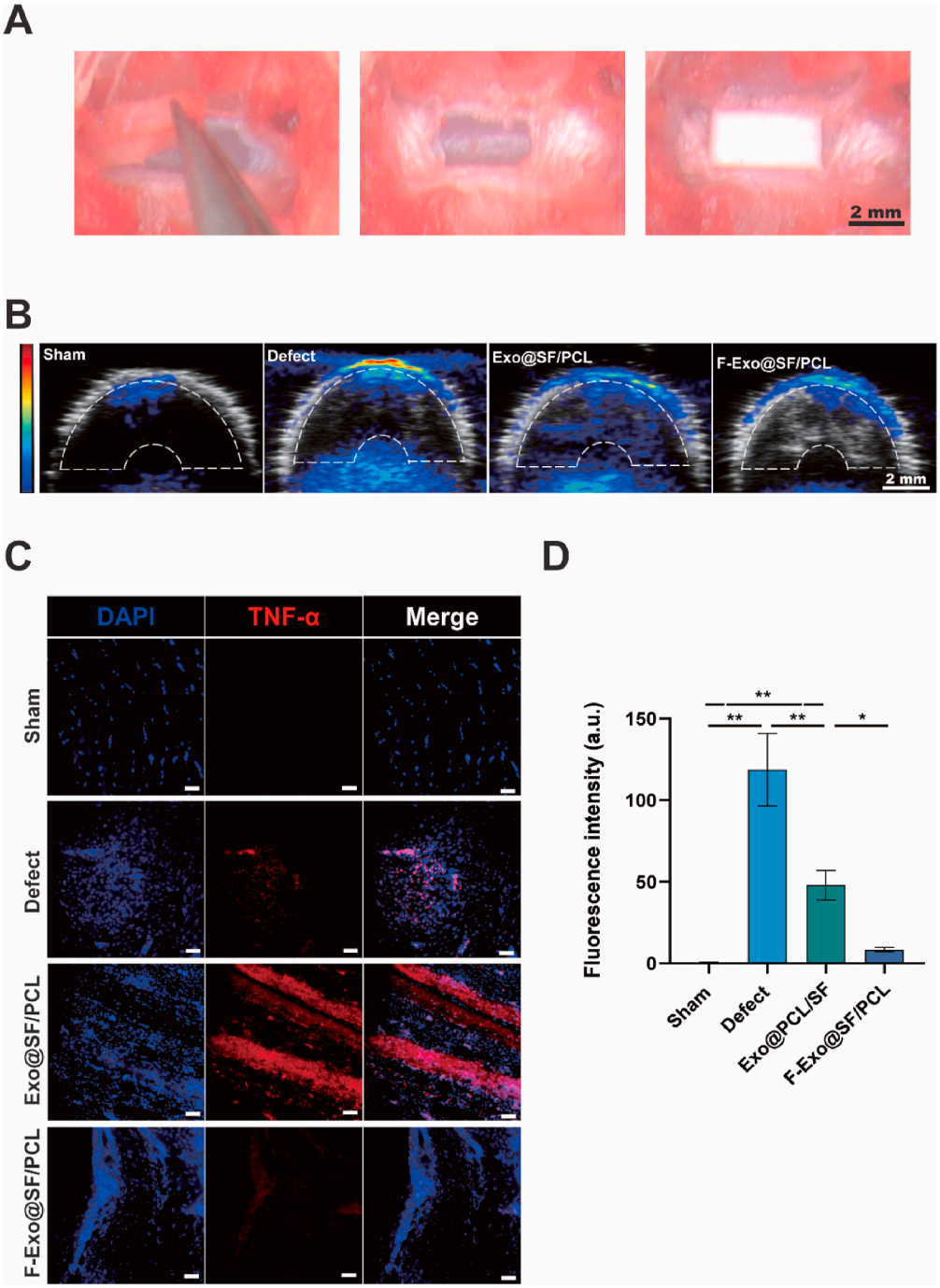

Fig. 5. F-Exo@SF/PCL scaffold effectively reduces ROS levels at the injury site of AF. (A) The procedure of implanting different types of scaffolds into the AF defect site. (B) The scavenging effect of F-Exo@SF/PCL scaffold on H_2O_2 at the AF injury site was evaluated using an H_2O_2 tracking probe, scale bar = 2 mm. (C) The anti-inflammatory effect of F-Exo@SF/PCL scaffold was assessed using TNF-α. Scale bar = 50 μm. (D) Quantification of fluorescence intensity of TNF-α in different groups. Data are presented as the mean ± SD, n = 3, $*p < 0.05$, $**p < 0.01$.

expression was detected from outside to inside in the defect group, invading along the direction of the tissue fissure. Although Exo@SF/PCL performed with a certain effectiveness in preventing vascular invasion, due to the poor integration between the scaffold and the AF tissue, vessels still invaded inside along the gap between the scaffold and the tissue. In contrast, F-Exo@SF/PCL was well integrated with the AF tissue, and only a small amount of CD31 was expressed inside (Fig. 7A).

Sirius red staining revealed that the defect AF exhibited a disorganized structure. While the Exo@SF/PCL scaffold integrated poorly with the native AF tissue, resulting in several obvious clefts. In contrast, the F-Exo@SF/PCL scaffold integrated well with the native AF tissue, forming a tight connection between the scaffold and the surrounding tissue (Fig. 7B). SEM was used to evaluate the integration of the scaffold with the adjacent AF tissue. The ECM structure of the defect group was loose, and many collagen fibers were broken. While the Exo@SF/PCL scaffold was able to achieve partial integration with the surrounding tissue, there were still many clefts between the scaffold and the tissue (indicated by yellow arrows). Conversely, F-Exo@SF/PCL demonstrated superior integration with the AF tissue, and few voids appeared between the scaffold and the tissue (Fig. 7B).

AFM was used to examine the mechanical strength of the scaffold-tissue integration interface. The results showed that the elastic

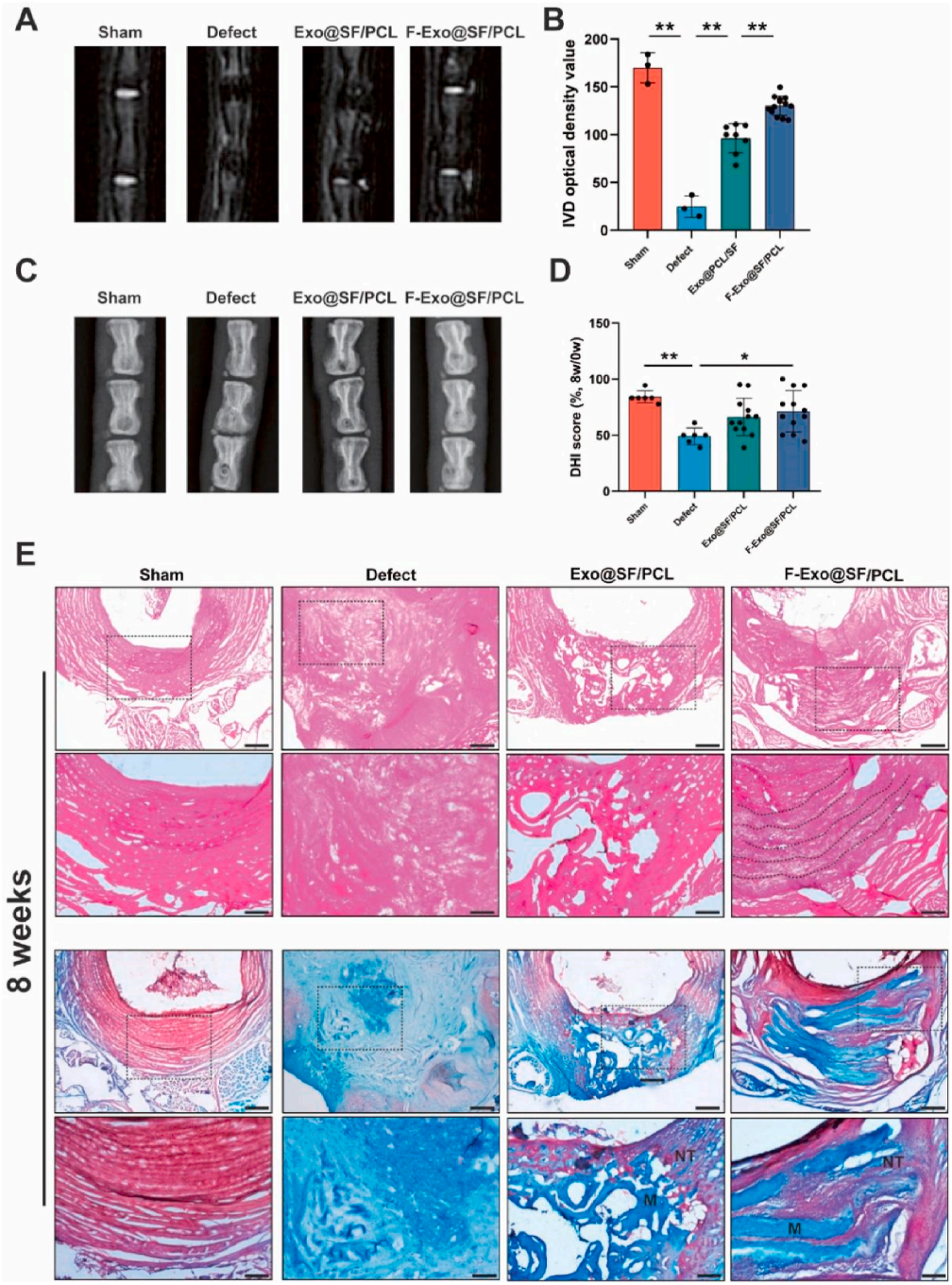

Fig. 6. F-Exo@SF/PCL scaffold prevents IVD herniation. (A) MRI analysis of T2 signals in different groups at 8 weeks. (B) Quantification of IVD optical density value in different groups. Data are presented as the mean ± SD, n = 3 for sham, n = 3 for defect, n = 8 for Exo@SF/PCL, and n = 13 for F-Exo@SF/PCL. $^{**}p < 0.01$. (C) X-ray analysis of IVDs in different groups. (D) Quantification of DHI score in different groups. Data are presented as the mean ± SD, n = 6 for sham, n = 6 for defect, and n = 12 for Exo@SF/PCL, n = 12 for F-Exo@SF/PCL. $^{*}p < 0.05$, $^{**}p < 0.01$. (E) H&E and SO/FG staining for evaluating the effect of F-Exo@SF/PCL scaffold on preventing IVD herniation (M: material, NT: native tissue). Scale bar = 100 μm (zoom out), scale bar = 200 μm (zoom in).

modulus of the defect AF was significantly decreased compared with the sham group. However, the elastic modulus of the scaffold-tissue interface did not improve after Exo@SF/PCL scaffold implantation, primarily because of the poor connection between the scaffold and the AF tissue. Conversely, the F-Exo@SF/PCL scaffold performed significantly better in the mechanical strength at the integration interface (Fig. 7D).

Overall, these findings suggested that the F-Exo@SF/PCL scaffold promoted scaffold-tissue integration, enhanced the mechanical strength of the scaffold-tissue integration interface, and effectively prevented external vascular invasion.

4. Discussion

Ensuring good integration is crucial for successful grafting, as it stabilizes the implant and enables it to function competently in vivo [42,43]. To achieve this, the implant and natural tissue must form sufficient connections to provide the necessary mechanical strength, otherwise the implantation will likely fail [44–46]. During cartilage repair, for example, large cracks between the implant and the natural tissue usually occur, which can lead to implant dislodgement and even induce immune rejection [47]. Healthy IVDs rely on the AF to maintain the position of

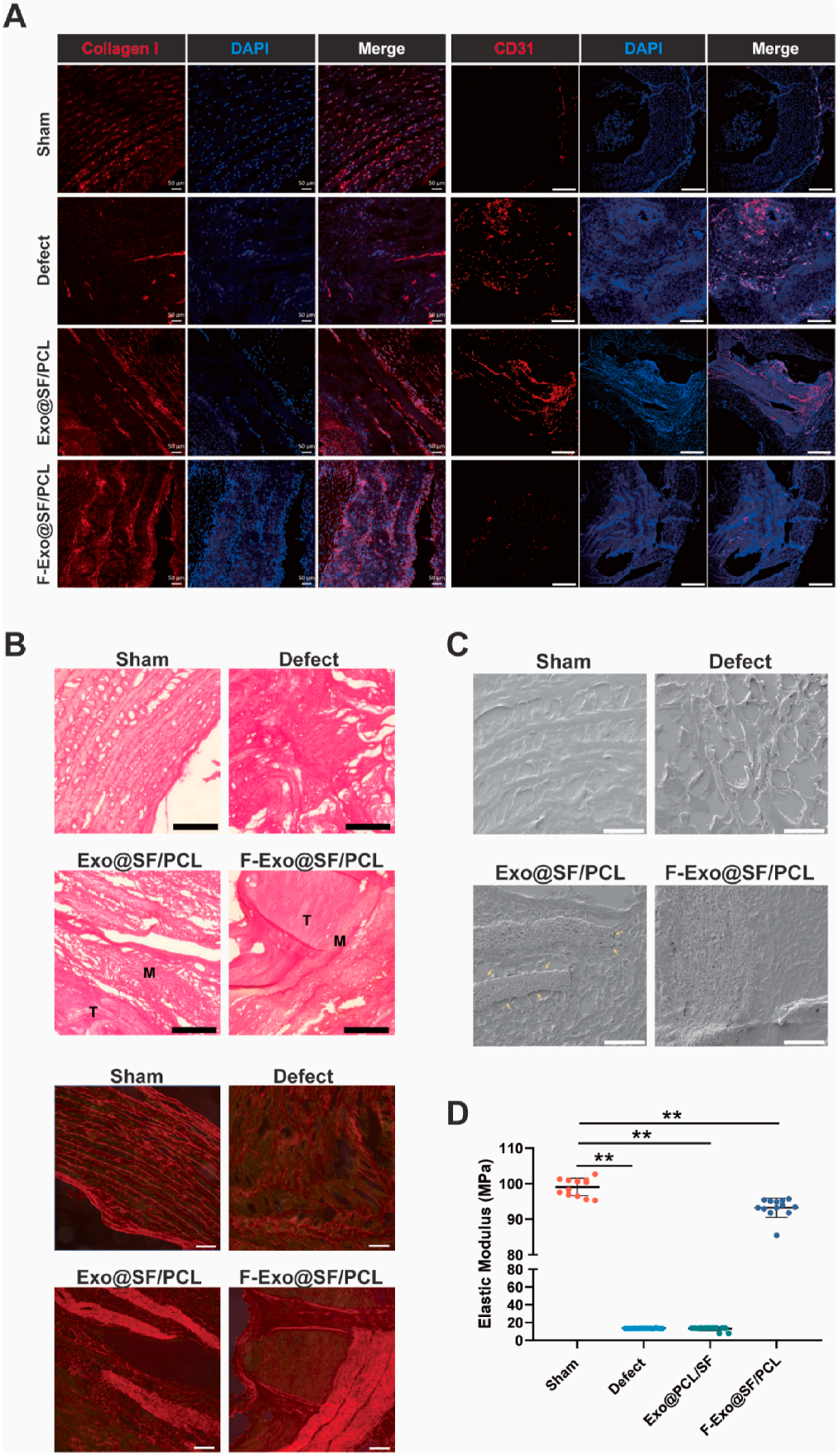

(caption on next page)

Fig. 7. F-Exo@SF/PCL scaffold promotes scaffold-tissue integration and effectively prevents external vascular invasion. (A) Immunofluorescent staining collagen I and CD31 in different groups at 8 weeks. Scale bar = 50 μm (left), scale bar = 200 μm (right). (B) Sirius red staining (bright and polarized light) in different groups at 8 weeks (M: material, T: tissue). Scale bar = 200 μm (bright); scale bar = 100 μm (polarized light). (C) SEM analysis of the morphology of ECM in different groups. (D) Quantification of mechanical properties in different groups. Data are presented as the mean ± SD, n = 13, $^{**}p < 0.01$.

the NP and the stability of the entire disc [3]. Thus, the formation of a stable integration between the scaffold and the AF tissue is essential for the AF to perform its biological function. Previous studies have used collagen hydrogel to prevent an outflow of NP tissue from AF injury sites [48]. However, the injury site still has fissures that impair the structural stability of the AF, partly because of the fast hydrogel degradation. This suggests using polymer compounds that degrade more slowly would be an appropriate strategy. Gluais et al. implanted an aligned PCL nanofiber scaffold into a sheep lumbar disc to evaluate the effect of the scaffold on AF repair in vivo. It was demonstrated that the polymer scaffold could mimic the AF structure. The PCL scaffold avoided outflow NP by integrating with the surrounding AF tissue [15]. A good integration of the scaffold with the tissue is achieved by cross-linking of ECM at the integration interface [49]. LOX has been demonstrated to catalyze the cross-linking of collagen and elastin, which can increase the mechanical strength of ECM. Athanasiou et al. used LOX to promote the integration of engineered cartilage with native cartilage and enhance the mechanical strength of the integration interface [50]. Therefore, we hypothesized that LOX could play a similar role in AF repair. The AFM results showed that LOX promoted the integration at the scaffold-tissue interface, significantly enhancing its mechanical strength, which contributed to the structural stability of the entire AF. The histological results indicated that the F-Exo@SF/PCL scaffold effectively sealed the defect AF area and prevented NP leakage. After AF damage, blood vessels from the periphery of the IVD can grow into the disc through structural AF clefts, exacerbating further disc degeneration [17,18]. After staining with the endothelial cell marker CD31, our result indicated that the F-Exo@SF/PCL scaffold achieved close integration between the scaffold and tissue, which significantly prevented the peripheral blood vessel invasion.

However, the short duration of LOX activity restricts its long-term application in vivo, making genetic engineering an alternative strategy for delivering the LOX gene into cells. Conventional delivery vectors, such as viral and non-viral vectors, have drawbacks, including viral vectors' immunogenicity and pathogenic risk, and non-viral vectors' insufficient transfection efficiency and cytotoxicity [51–53]. The emergence of exosomes provides a new possibility for gene delivery. Exosomes, which are secreted by cells, are 30–150 nm vesicles that transmit proteins, genetic information, and other biological substances between cells [54,55]. Recently, exosomes have been widely employed in tissue engineering strategies. Lee et al. designed autologous exosomes containing a cocktail of reprogramming factors that converted fibroblasts into neural progenitor cells [56]. Exosomes are natural products; thus, the modification process must avoid disrupting their structure and biological function. Herein, a click chemistry strategy was used as it is a bioorthogonal chemistry that is commonly used to label exosomes. Song et al. co-cultured A549 cells with Ac4ManNAz to obtain surface azide-modified exosomes (Az-EVs) [57]. Furthermore, Xing et al. modified the surface of collagen fibers with DBCO and clicked Az-EVs onto the surface of collagen fibers using an alkyne-azide coupling reaction [58]. In this study, we co-cultured Ac4ManNAz with BMSCs, isolated the azide-modified exosomes, and mixed them with DBCO-modified SF/PCL scaffolds. Using DiI to label exosomes, it was observed that exosomes could be uniformly clicked onto the scaffold surface. AFCs were cultured on the scaffold, and the results indicated that the cells could take up exosomes, resulting in nearly 40% of exogenous LOX-positive cells. These results suggest that this system can modify exosomes stably, and exosomes can serve as delivery vectors to achieve efficient target gene transfection.

In addition, injury sites are often accompanied by enhanced ROS level, which can result in metabolic disorders and cellular apoptosis, ultimately hindering tissue repair. The use of MnO_2 to decompose H_2O_2 is a typical approach for removing ROS. Therefore, we prepared MnO_2 NPs that were bonded to a scaffold through physical adsorption. To trace the H_2O_2 in vivo, we used the Lipo@HRP&ABTS nanoprobe to visualize the H_2O_2 level at the AF injury site [59]. Using PA imaging, we observed that MnO_2 NPs led to a significant reduction in H_2O_2 levels at the injury sites. An interesting finding was that the MnO_2 NPs down-regulated the gene expression of CAT, MnSOD and ECSOD, which contradicts previous studies [60]. This unexpected result may be due to the ability of MnO2 NPs remove ROS efficiency and sensitively, allowing the levels of MnSOD and ECSOD to return to equilibrium with ROS. On the other hand, CAT requires a longer response time to excessive ROS levels [61]; however, its expression level was only evaluated after 24 h in this study.

In addition to AF repair, most scaffolds that are utilized in different tissue regeneration strategies may have the possibility of poor integration with the host tissue. A lack of integration at the scaffold-tissue interface can lead to secondary injury, chronic pain, and even implant removal, which severely impairs tissue regeneration [62–64]. The scaffold designed in this study is not only used in AF repair but can also be used in other tissue repair strategies. First, electrospinning-made polymer scaffolds can be maintained for a long time in vivo, which can overcome the poor scaffold-tissue integration due to the fast degradation of the scaffold. Second, the utilization of LOX is unique in this scaffold for promoting scaffold-tissue integration. Compared with artificial chemical bonds, the catalytic process of collagen cross-linking by LOX is natural in the body, which avoids the toxicity caused by the chemicals. One possible application is using it as a bionic periosteum. A crucial factor of bionic periosteum that induces bone regeneration is that the functional scaffold should be well integrated with the bone [65]. Except for promoting the integration of scaffold-bone interfaces, our multifunctional scaffold can load growth factors such as vascular endothelial growth factor (VEGF) or bone morphogenetic protein-2 (BMP-2). This modified multifunctional scaffold may perform a therapeutic effect in bone regeneration.

5. Conclusion

Good integration between the implanted scaffold and adjacent tissue is a crucial prerequisite for promoting AF repair. Promoting collagen cross-linking at the scaffold-tissue interface is an effective strategy. To achieve this, we developed a multifunctional scaffold containing loaded LOX pDNA exosomes and MnO_2 NPs. LOX facilitates extracellular matrix crosslinking, while MnO_2 NPs inhibit excessive ROS-induced extracellular matrix degradation at the injury site, enhancing the crosslinking effect of LOX. The multifunctional scaffold promoted collagen cross-linking at the scaffold-tissue interface, restored mechanical strength, and prevented external vascular infiltration. Different from the approach of promoting matrix generation, this study emphasizes the important role of matrix cross-linking in AF repair, providing novel insights applicable to diverse tissue repairs, including AF. Moreover, this multifunctional scaffold presents a versatile gene delivery platform with broad potential for other tissue repairs.

Ethics approval and consent to participate

The protocol listed below has been reviewed and approved by the Ethics Committee of Soochow University (ECSU), and the Approval Number is SUDA202209013A01.

CRediT authorship contribution statement

Runze Zhao: Writing – review & editing, Writing – original draft, Methodology, Investigation, Funding acquisition, Formal analysis, Conceptualization. **Feng Han:** Writing – review & editing, Methodology, Investigation, Formal analysis, Conceptualization. **Qifan Yu:** Writing – review & editing, Methodology, Funding acquisition, Formal analysis. **Zhuang Zhu:** Writing – review & editing, Software, Methodology, Formal analysis. **Zhengdong Tu:** Writing – review & editing, Methodology. **Tingting Xia:** Writing – review & editing, Supervision, Project administration, Methodology, Funding acquisition, Formal analysis, Conceptualization. **Bin Li:** Writing – review & editing, Supervision, Project administration, Investigation, Funding acquisition, Conceptualization.

Declaration of competing interest

The authors declare that they have no known competing financial interests or personal relationships that could have appeared to influence the work reported in this paper.

Acknowledgements

This work was supported by the National Natural Science Foundation of China (32201115, 32130059, 81925027). Suzhou Science and Technology Development Plan Project (SKY2022100). Gusu Health Talents Program of Suzhou Municipal Health Commission (GSWS2021070). Postgraduate Research &Practice Innovation Program of Jiangsu Province (KYCX23_3269) and the Priority Academic Program Development of Jiangsu Higher Education Institutions.

Appendix A. Supplementary data

Supplementary data to this article can be found online at https://doi.org/10.1016/j.bioactmat.2024.03.007.

References

[1] F. Yang, W. Liu, Y. Huang, S. Yang, Z. Shao, X. Cai, L. Xiong, Regulated cell death: implications for intervertebral disc degeneration and therapy, J Orthop Translat 37 (2022) 163–172.
[2] N. Newell, J.P. Little, A. Christou, M.A. Adams, C.J. Adam, S.D. Masouros, Biomechanics of the human intervertebral disc: a review of testing techniques and results, J. Mech. Behav. Biomed. Mater. 69 (2017) 420–434.
[3] Z. Wang, X. Jin, B. Zhang, J. Kong, R. Deng, K. Wu, L. Xie, X. Liu, R. Kang, Stress stimulation maintaining by genipin crosslinked hydrogel promotes annulus fibrosus healing, J Orthop Translat 40 (2023) 104–115.
[4] M. Ghannam, F. Jumah, S. Mansour, A. Samara, S. Alkhdour, M.A. Alzuabi, L. Aker, N. Adeeb, J. Massengale, R.J. Oskouian, R.S. Tubbs, Surgical anatomy, radiological features, and molecular biology of the lumbar intervertebral discs, Clin. Anat. 30 (2) (2017) 251–266.
[5] L.J. Smith, N.L. Nerurkar, K.S. Choi, B.D. Harfe, D.M. Elliott, Degeneration and regeneration of the intervertebral disc: lessons from development, Dis Model Mech 4 (1) (2011) 31–41.
[6] J.X. Chen, Y.H. Li, J. Wen, Z. Li, B.S. Yu, Y.C. Huang, Annular defects impair the mechanical stability of the intervertebral disc, Global Spine J. 13 (3) (2023) 724–729.
[7] S. Molladavoodi, J. McMorran, D. Gregory, Mechanobiology of annulus fibrosus and nucleus pulposus cells in intervertebral discs, Cell Tissue Res. 379 (3) (2020) 429–444.
[8] Global, regional, and national incidence, prevalence, and years lived with disability for 354 diseases and injuries for 195 countries and territories, 1990-2017: a systematic analysis for the Global Burden of Disease Study 2017, Lancet 392 (10159) (2018) 1789–1858.
[9] L. Wang, H. Ye, Z. Li, C. Lu, J. Ye, M. Liao, X. Chen, Epidemiological trends of low back pain at the global, regional, and national levels, Eur. Spine J. 31 (4) (2022) 953–962.
[10] E. Kague, F. Turci, E. Newman, Y. Yang, K.R. Brown, M.S. Aglan, G.A. Otaify, S. A. Temtamy, V.L. Ruiz-Perez, S. Cross, C.P. Royall, P.E. Witten, C.L. Hammond, 3D assessment of intervertebral disc degeneration in zebrafish identifies changes in bone density that prime disc disease, Bone Res 9 (1) (2021) 39.
[11] N.N. Knezevic, K.D. Candido, J.W.S. Vlaeyen, J. Van Zundert, S.P. Cohen, Low back pain, Lancet 398 (10294) (2021) 78–92.
[12] F. Yang, W. Liu, Y. Huang, S. Yang, Z. Shao, X. Cai, L. Xiong, Regulated cell death: implications for intervertebral disc degeneration and therapy, J Orthop Translat 37 (2022) 163–172.
[13] M.J. McGirt, G.L. Ambrossi, G. Datoo, D.M. Sciubba, T.F. Witham, J.P. Wolinsky, Z. L. Gokaslan, A. Bydon, Recurrent disc herniation and long-term back pain after primary lumbar discectomy: review of outcomes reported for limited versus aggressive disc removal, Neurosurgery 64 (2) (2009) 338–344. ; discussion 344-5.
[14] E.J. Carragee, A.O. Spinnickie, T.F. Alamin, S. Paragioudakis, A prospective controlled study of limited versus subtotal posterior discectomy: short-term outcomes in patients with herniated lumbar intervertebral discs and large posterior anular defect, Spine 31 (6) (2006) 653–657.
[15] M. Gluais, J. Clouet, M. Fusellier, C. Decante, C. Moraru, M. Dutilleul, J. Veziers, J. Lesoeur, D. Dumas, J. Abadie, A. Hamel, E. Bord, S.Y. Chew, J. Guicheux, C. Le Visage, In vitro and in vivo evaluation of an electrospun-aligned microfibrous implant for Annulus fibrosus repair, Biomaterials 205 (2019) 81–93.
[16] A.H. Shamsah, S.H. Cartmell, S.M. Richardson, L.A. Bosworth, Tissue engineering the annulus fibrosus using 3D rings of electrospun PCL:PLLA angle-ply nanofiber sheets, Front. Bioeng. Biotechnol. 7 (2019) 437.
[17] P. Lama, C.L. Le Maitre, I.J. Harding, P. Dolan, M.A. Adams, Nerves and blood vessels in degenerated intervertebral discs are confined to physically disrupted tissue, J. Anat. 233 (1) (2018) 86–97.
[18] J. Melrose, S. Roberts, S. Smith, J. Menage, P. Ghosh, Increased nerve and blood vessel ingrowth associated with proteoglycan depletion in an ovine anular lesion model of experimental disc degeneration, Spine 27 (12) (2002) 1278–1285.
[19] W. Kong, C. Lyu, H. Liao, Y. Du, Collagen crosslinking: effect on structure, mechanics and fibrosis progression, Biomed. Mater. 16 (6) (2021).
[20] L.I. Smith-Mungo, H.M. Kagan, Lysyl oxidase: properties, regulation and multiple functions in biology, Matrix Biol. 16 (7) (1998) 387–398.
[21] K. Csiszar, Lysyl oxidases: a novel multifunctional amine oxidase family, Prog. Nucleic Acid Res. Mol. Biol. 70 (2001) 1–32.
[22] S.D. Vallet, S. Ricard-Blum, Lysyl oxidases: from enzyme activity to extracellular matrix cross-links, Essays Biochem. 63 (3) (2019) 349–364.
[23] X.X. Nguyen, T. Nishimoto, T. Takihara, L. Mlakar, A.D. Bradshaw, C. Feghali-Bostwick, Lysyl oxidase directly contributes to extracellular matrix production and fibrosis in systemic sclerosis, Am. J. Physiol. Lung Cell Mol. Physiol. 320 (1) (2021) L29–l40.
[24] R. Zhao, W. Liu, M. Wang, Y. Zhang, L. Pan, F. Feng, T. Xia, L. Yang, Lysyl oxidase inhibits TNF-α induced rat nucleus pulposus cell apoptosis via regulating Fas/FasL pathway and the p53 pathways, Life Sci. 260 (2020) 118483.
[25] M. Kou, L. Huang, J. Yang, Z. Chiang, S. Chen, J. Liu, L. Guo, X. Zhang, X. Zhou, X. Xu, X. Yan, Y. Wang, J. Zhang, A. Xu, H.F. Tse, Q. Lian, Mesenchymal stem cell-derived extracellular vesicles for immunomodulation and regeneration: a next generation therapeutic tool? Cell Death Dis. 13 (7) (2022) 580.
[26] S. Varderidou-Minasian, M.J. Lorenowicz, Mesenchymal stromal/stem cell-derived extracellular vesicles in tissue repair: challenges and opportunities, Theranostics 10 (13) (2020) 5979–5997.
[27] R. Kalluri, V.S. LeBleu, The biology, function, and biomedical applications of exosomes, Science 367 (6478) (2020).
[28] Q. Guo, D. Zhu, Y. Wang, Z. Miao, Z. Chen, Z. Lin, J. Lin, C. Huang, L. Pan, L. Wang, S. Zeng, J. Wang, X. Zheng, Y. Lin, X. Zhang, Y. Wu, Targeting STING attenuates ROS induced intervertebral disc degeneration, Osteoarthritis Cartilage 29 (8) (2021) 1213–1224.
[29] Y. Li, L. Chen, Y. Gao, X. Zou, F. Wei, Oxidative stress and intervertebral disc degeneration: pathophysiology, signaling pathway, and therapy, Oxid. Med. Cell. Longev. 2022 (2022) 1984742.
[30] S. Suzuki, N. Fujita, N. Hosogane, K. Watanabe, K. Ishii, Y. Toyama, K. Takubo, K. Horiuchi, T. Miyamoto, M. Nakamura, M. Matsumoto, Excessive reactive oxygen species are therapeutic targets for intervertebral disc degeneration, Arthritis Res. Ther. 17 (2015) 316.
[31] L. Kang, Q. Xiang, S. Zhan, Y. Song, K. Wang, K. Zhao, S. Li, Z. Shao, C. Yang, Y. Zhang, Restoration of autophagic flux rescues oxidative damage and mitochondrial dysfunction to protect against intervertebral disc degeneration, Oxid. Med. Cell. Longev. 2019 (2019) 7810320.
[32] H. Deng, W. Yang, Z. Zhou, R. Tian, L. Lin, Y. Ma, J. Song, X. Chen, Targeted scavenging of extracellular ROS relieves suppressive immunogenic cell death, Nat. Commun. 11 (1) (2020) 4951.
[33] A. Robson, Oxidation of miRNAs by ROS leads to cardiac hypertrophy, Nat. Rev. Cardiol. 17 (11) (2020) 678.
[34] P. Prasad, C.R. Gordijo, A.Z. Abbasi, A. Maeda, A. Ip, A.M. Rauth, R.S. DaCosta, X. Y. Wu, Multifunctional albumin-MnO_2 nanoparticles modulate solid tumor microenvironment by attenuating hypoxia, acidosis, vascular endothelial growth factor and enhance radiation response, ACS Nano 8 (4) (2014) 3202–3212.
[35] D.B. Broughton, R.L. Wentworth, M.E. Laing, Mechanism of decomposition of hydrogen peroxide solutions with manganese dioxide, J. Am. Chem. Soc. 69 (4) (1947) 744–747.
[36] S. Kumar, I.M. Adjei, S.B. Brown, O. Liseth, B. Sharma, Manganese dioxide nanoparticles protect cartilage from inflammation-induced oxidative stress, Biomaterials 224 (2019) 119467.
[37] Y. Qian, L. Li, Y. Song, L. Dong, P. Chen, X. Li, K. Cai, O. Germershaus, L. Yang, Y. Fan, Surface modification of nanofibrous matrices via layer-by-layer functionalized silk assembly for mitigating the foreign body reaction, Biomaterials 164 (2018) 22–37.
[38] M. Song, T. Liu, C. Shi, X. Zhang, X. Chen, Bioconjugated manganese dioxide nanoparticles enhance chemotherapy response by priming tumor-associated macrophages toward M1-like phenotype and attenuating tumor hypoxia, ACS Nano 10 (1) (2016) 633–647.

[39] Y. Luo, Preparation of MnO2 nanoparticles by directly mixing potassium permanganate and polyelectrolyte aqueous solutions, Mater. Lett. 61 (8–9) (2007) 1893–1895.
[40] Y. Peng, X. Qing, H. Shu, S. Tian, W. Yang, S. Chen, H. Lin, X. Lv, L. Zhao, X. Chen, F. Pu, D. Huang, X. Cao, Z. Shao, Proper animal experimental designs for preclinical research of biomaterials for intervertebral disc regeneration, Biomater Transl 2 (2) (2021) 91–142.
[41] T. Liang, Y.J. Che, X. Chen, H.T. Li, H.L. Yang, Z.P. Luo, Nano and micro biomechanical alterations of annulus fibrosus after in situ immobilization revealed by atomic force microscopy, J. Orthop. Res. 37 (1) (2019) 232–238.
[42] L. Li, Y. Qian, C. Jiang, Y. Lv, W. Liu, L. Zhong, K. Cai, S. Li, L. Yang, The use of hyaluronan to regulate protein adsorption and cell infiltration in nanofibrous scaffolds, Biomaterials 33 (12) (2012) 3428–3445.
[43] R. Sridharan, A.R. Cameron, D.J. Kelly, C.J. Kearney, F.J. O'Brien, Biomaterial based modulation of macrophage polarization: a review and suggested design principles, Mater. Today 18 (6) (2015) 313–325.
[44] M. Gasik, Understanding biomaterial-tissue interface quality: combined in vitro evaluation, Sci. Technol. Adv. Mater. 18 (1) (2017) 550–562.
[45] Y. Song, L. Li, W. Zhao, Y. Qian, L. Dong, Y. Fang, L. Yang, Y. Fan, Surface modification of electrospun fibers with mechano-growth factor for mitigating the foreign-body reaction, Bioact. Mater. 6 (9) (2021) 2983–2998.
[46] L. Yang, X. Lin, J. Zhou, S. Hou, Y. Fang, X. Bi, L. Yang, L. Li, Y. Fan, Cell membrane-biomimetic coating via click-mediated liposome fusion for mitigating the foreign-body reaction, Biomaterials 271 (2021) 120768.
[47] E.K. Moo, P. Tanska, S. Federico, Y. Al-Saffar, W. Herzog, R.K. Korhonen, Collagen fibres determine the crack morphology in articular cartilage, Acta Biomater. 126 (2021) 301–314.
[48] B. Borde, P. Grunert, R. Härtl, L.J. Bonassar, Injectable, high-density collagen gels for annulus fibrosus repair: an in vitro rat tail model, J. Biomed. Mater. Res. 103 (8) (2015) 2571–2581.
[49] J. Chakraborty, S. Roy, S. Murab, R. Ravani, K. Kaur, S. Devi, D. Singh, S. Sharma, S. Mohanty, A.K. Dinda, R. Tandon, S. Ghosh, Modulation of macrophage phenotype, maturation, and graft integration through chondroitin sulfate cross-linking to decellularized cornea, ACS Biomater. Sci. Eng. 5 (1) (2019) 165–179.
[50] E.A. Makris, R.F. MacBarb, N.K. Paschos, J.C. Hu, K.A. Athanasiou, Combined use of chondroitinase-ABC, TGF-β1, and collagen crosslinking agent lysyl oxidase to engineer functional neotissues for fibrocartilage repair, Biomaterials 35 (25) (2014) 6787–6796.
[51] M.H. Butt, M. Zaman, A. Ahmad, R. Khan, T.H. Mallhi, M.M. Hasan, Y.H. Khan, S. Hafeez, E.E.S. Massoud, M.H. Rahman, S. Cavalu, Appraisal for the potential of viral and nonviral vectors in gene therapy: a review, Genes 13 (8) (2022).
[52] H. Zu, D. Gao, Non-viral vectors in gene therapy: recent development, challenges, and prospects, AAPS J. 23 (4) (2021) 78.
[53] J.R. Mendell, S.A. Al-Zaidy, L.R. Rodino-Klapac, K. Goodspeed, S.J. Gray, C.N. Kay, S.L. Boye, S.E. Boye, L.A. George, S. Salabarria, M. Corti, B.J. Byrne, J.P. Tremblay, Current clinical applications of in vivo gene therapy with AAVs, Mol. Ther. 29 (2) (2021) 464–488.
[54] Y. Liang, L. Duan, J. Lu, J. Xia, Engineering exosomes for targeted drug delivery, Theranostics 11 (7) (2021) 3183–3195.
[55] Y. Liang, X. Xu, X. Li, J. Xiong, B. Li, L. Duan, D. Wang, J. Xia, Chondrocyte-Targeted MicroRNA delivery by engineered exosomes toward a cell-free osteoarthritis therapy, ACS Appl. Mater. Interfaces 12 (33) (2020) 36938–36947.
[56] Y.S. Lee, W.Y. Jung, H. Heo, M.G. Park, S.H. Oh, B.G. Park, S. Kim, Exosome-Mediated ultra-effective direct conversion of human fibroblasts into neural progenitor-like cells, ACS Nano 12 (3) (2018) 2531–2538.
[57] S. Song, M.K. Shim, S. Lim, Y. Moon, S. Yang, J. Kim, Y. Hong, H.Y. Yoon, I.S. Kim, K.Y. Hwang, K. Kim, In situ one-step fluorescence labeling strategy of exosomes via bioorthogonal click chemistry for real-time exosome tracking in vitro and in vivo, Bioconjugate Chem. 31 (5) (2020) 1562–1574.
[58] Y. Xing, S.S. Yerneni, W. Wang, R.E. Taylor, P.G. Campbell, X. Ren, Engineering pro-angiogenic biomaterials via chemoselective extracellular vesicle immobilization, Biomaterials 281 (2022) 121357.
[59] Q. Chen, C. Liang, X. Sun, J. Chen, Z. Yang, H. Zhao, L. Feng, Z. Liu, H(2)O(2)-responsive liposomal nanoprobe for photoacoustic inflammation imaging and tumor theranostics via in vivo chromogenic assay, Proc Natl Acad Sci U S A 114 (21) (2017) 5343–5348.
[60] J. Li, F. Han, J. Ma, H. Wang, J. Pan, G. Yang, H. Zhao, J. Zhao, J. Liu, Z. Liu, Targeting endogenous hydrogen peroxide at bone defects promotes bone repair, Adv. Funct. Mater. 32 (10) (2022) 2111208.
[61] M. Mathy-Hartert, L. Hogge, C. Sanchez, G. Deby-Dupont, J.M. Crielaard, Y. Henrotin, Interleukin-1beta and interleukin-6 disturb the antioxidant enzyme system in bovine chondrocytes: a possible explanation for oxidative stress generation, Osteoarthritis Cartilage 16 (7) (2008) 756–763.
[62] B.T. Heniford, A. Park, B.J. Ramshaw, G. Voeller, Laparoscopic repair of ventral hernias: nine years' experience with 850 consecutive hernias, Ann. Surg. 238 (3) (2003) 391–399. ; discussion 399-400.
[63] S. Kumar, R.G. Wilson, S.J. Nixon, I.M. Macintyre, Chronic pain after laparoscopic and open mesh repair of groin hernia, Br. J. Surg. 89 (11) (2002) 1476–1479.
[64] R. Rosch, P. Lynen-Jansen, K. Junge, M. Knops, B. Klosterhalfen, U. Klinge, P. R. Mertens, V. Schumpelick, Biomaterial-dependent MMP-2 expression in fibroblasts from patients with recurrent incisional hernias, Hernia 10 (2) (2006) 125–130.
[65] W. Zhang, N. Wang, M. Yang, T. Sun, J. Zhang, Y. Zhao, N. Huo, Z. Li, Periosteum and development of the tissue-engineered periosteum for guided bone regeneration, J Orthop Translat 33 (2022) 41–54.